



Structure and mechanism of NALCN-FAM155A-UNC79-UNC80 channel complex

Yunlu Kang ^{1,2} & Lei Chen ^{1,2,3,4}✉

NALCN channel mediates sodium leak currents and is important for maintaining proper resting membrane potential. NALCN and FAM155A form the core complex of the channel, the activity of which essentially depends on the presence of both UNC79 and UNC80, two auxiliary proteins. NALCN, FAM155A, UNC79, and UNC80 co-assemble into a large heterotetrameric channel complex. Genetic mutations of NALCN channel components lead to neurodevelopmental diseases. However, the structure and mechanism of the intact channel complex remain elusive. Here, we present the cryo-EM structure of the mammalian NALCN-FAM155A-UNC79-UNC80 quaternary complex. The structure shows that UNC79-UNC80 form a large piler-shaped heterodimer which was tethered to the intracellular side of the NALCN channel through tripartite interactions with the cytoplasmic loops of NALCN. Two interactions are essential for proper cell surface localization of NALCN. The other interaction relieves the self-inhibition of NALCN by pulling the auto-inhibitory CTD Interacting Helix (CIH) out of its binding site. Our work defines the structural mechanism of NALCN modulation by UNC79 and UNC80.

¹State Key Laboratory of Membrane Biology, College of Future Technology, Institute of Molecular Medicine, Peking University, Beijing Key Laboratory of Cardiometabolic Molecular Medicine, Beijing 100871, China. ²National Biomedical Imaging Center, Peking University, Beijing 100871, China. ³Peking-Tsinghua Center for Life Sciences, Peking University, Beijing 100871, China. ⁴Academy for Advanced Interdisciplinary Studies, Peking University, Beijing 100871, China. ✉email: chenlei2016@pku.edu.cn

NALCN channel mediates voltage-modulated sodium leak currents which can be blocked by extracellular calcium¹. It is essential for maintaining the proper resting membrane potential, and thus the electrical excitability of certain cells². The mutations in the NALCN gene lead to genetic diseases such as Infantile Hypotonia with Psychomotor Retardation and Characteristic Facies 1 (IHPRF1; OMIM 615419)^{3,4} and Congenital Contractures of the Limbs and Face, Hypotonia, and Developmental Delay (CLIFAHDD; OMIM 616266)⁵. Mice lacking the NALCN gene are neonatal lethal due to respiratory rhythm defects⁶, while the gain-of-function mutation of NALCN impairs rapid eye movement sleep and causes the *dreamless* phenotype in mouse⁷.

The functional NALCN channel is a hetero-tetrameric channelosome that is composed of NALCN, FAM155, UNC79, and UNC80 proteins, with a total molecular weight of 920 kDa¹. The co-expression of these four proteins is necessary and sufficient to reconstitute robust NALCN currents in a heterologous system such as *Xenopus* oocyte and HEK293 cells¹. NALCN protein is the pore-forming subunit of the complex and shares sequence and structural homology with eukaryotic voltage-gated sodium channels (Na_v) and calcium channels (Ca_v)⁸. FAM155 proteins are transmembrane proteins with a cysteine-rich domain. They are important for the membrane localization of NALCN⁹. UNC79 and UNC80 are large proteins without any known domains but are important for the function of NALCN^{10–12}. UNC79 and UNC80 facilitate robust currents of NALCN in a heterologous expression system, such as HEK293T cells or *Xenopus* oocyte¹. In agreement with this, genetic mutations of the UNC80 gene also lead to IHPRF diseases (IHPRF2; OMIM 616801) in human¹³, and knock-out of UNC79 leads to disrupted breathing rhythms¹⁴, phenocopying the loss-of-function of the NALCN channel in mice⁶. Recently advances in the structure determination of mammalian NALCN-FAM155A subcomplex have provided insights into how FAM155A interacts with the NALCN channel, how the functional and degenerate voltage sensors are spatially arranged, and how the non-canonical selectivity filter allows the permeation of sodium^{15–17}. Moreover, our previous high-resolution structure identified a CTD-Interacting Helix (CIH) on the linker of NALCN domain II-III (D_{II-III})¹⁵. The interaction between CTD and CIH has never been observed in related Na_v or Ca_v channels previously. Despite the progress, these structural works were done using the NALCN-FAM155A subcomplex which is essentially not fully functional due to the absence of UNC79 and UNC80 subunits¹. Therefore, the structures of UNC79 and UNC80 and their regulatory mechanism on the NALCN channel remain enigmatic. In this work, we present the structure of the NALCN-FAM155A-UNC79-UNC80 hetero-tetrameric channel complex, providing structural insights into how UNC79 and UNC80 regulate the NALCN channel.

Results

Architecture of the NALCN-FAM155A-UNC79-UNC80 quaternary complex. Previous structural studies on the NALCN-FAM155A heterodimer showed that this subcomplex is well-folded in the absence of UNC79 and UNC80^{15–17}. However, both UNC79 and UNC80 are crucial for the NALCN currents in HEK293T cells¹, indicating that UNC79 and UNC80 might not be necessary for channel folding, but rather affect the plasma membrane localization of the channel or play other regulatory roles. We inserted the 3×HA tag after P1077 of NALCN which is on the extracellular loop between S5 and P1 helices of Domain III (D_{III}) and found that the insertion of the 3×HA tag does not affect the electrophysiological properties of the NALCN channel

(Supplementary Fig. 1a). Then we used an HA antibody to quantify the surface localization of NALCN¹⁸. We found that the NALCN-FAM155A subcomplex has little surface localization (Fig. 1a), which is consistent with the fact that little currents were observed when only NALCN and FAM155A were expressed¹. Co-expression of both UNC79 and UNC80 dramatically promoted the surface localization of NALCN (Fig. 1a), in agreement with markedly enhanced currents¹. These results collectively suggest that co-expression of UNC79 and UNC80 could promote the surface localization of the NALCN to enhance NALCN currents. To understand the underlying structural mechanism, we sought to obtain the NALCN-FAM155A-UNC79-UNC80 quaternary protein complex for cryo-EM studies. By screening the high-affinity binary interactions within the complex, we found that UNC79 and UNC80 subunits co-migrate on FSEC (Supplementary Fig. 1b), suggesting they could form a stable heterodimer. However, the quaternary complex tends to dissociate during purification^{16,17}, probably due to the low affinity between the NALCN-FAM155A subcomplex and UNC79-UNC80 heterodimer. To overcome this obstacle, we exploited the tight binding between GFP and its nanobody¹⁹. We fused GFP after the C-terminus of NALCN and fused nanobody (NbGFP) with the N-terminus of UNC80 to increase the affinity between NALCN-FAM155A and UNC79-UNC80 and to enhance the stability of the hetero-tetrameric complex (Supplementary Fig. 1c). We also included HA or FLAG tags in several subunits to facilitate their detection during protein expression and purification. We found that co-expression of NALCN-GFP, FAM155A-FLAG, NbGFP-UNC80, and HA-UNC79 conferred typical NALCN currents in HEK293T cells (Supplementary Fig. 1d), suggesting these constructs recapitulate the properties of NALCN and are suitable for studying the structural mechanism of the NALCN quaternary complex.

Subsequent protein purification and cryo-EM multi-body analysis showed relative motions between NALCN-FAM155A subcomplex and UNC79-UNC80 heterodimer (Supplementary Movie 1)²⁰. Moreover, there are significant conformational heterogeneity within the UNC79-UNC80 heterodimer revealed by 3D variability analysis (Supplementary Movie 2)²¹. Further extensive signal subtraction and focused refinements resolved five overlapping structural fragments at 2.9–3.7 Å resolution (Supplementary Figs. 2, 3 and Supplementary Table 1). These five maps covered all of the resolvable parts of the quaternary complex. The five maps from focused refinement were combined to generate the composite map for model building and interpretation. We exploited AlphaFold2 to aid the manual building of UNC79 and UNC80 models²². Our final model encompasses 1346 out of 1738 residues of NALCN, 173 out of 467 residues of FAM155A, 1528 out of 2654 residues of UNC79, and 1711 out of 3326 residues of UNC80 (Supplementary Table 1). The remaining unmodeled regions are probably highly disordered and therefore unresolvable in cryo-EM maps.

The structure of the NALCN-FAM155A subcomplex is similar to our previous structure at 2.65 Å with a root-mean-square deviation of 0.909 Å (Fig. 1b–f and Supplementary Fig. 8a)¹⁵. The UNC79-UNC80 heterodimer shows a large helix-rich structure in the cytosol. The NALCN-FAM155A subcomplex sits above the central joint of the UNC79-UNC80 heterodimer to form an asymmetric quaternary complex occupying 200 Å × 315 Å × 145 Å 3D space (Fig. 1b–f and Supplementary Movie 3).

Structure of the UNC79-UNC80 heterodimer. We resolved 72 cytosolic helices for UNC79 and 77 helices for UNC80 in total (Supplementary Figs. 4, 5). These cytosolic helices further pack into HAET repeats and ARM repeats which act as basic building

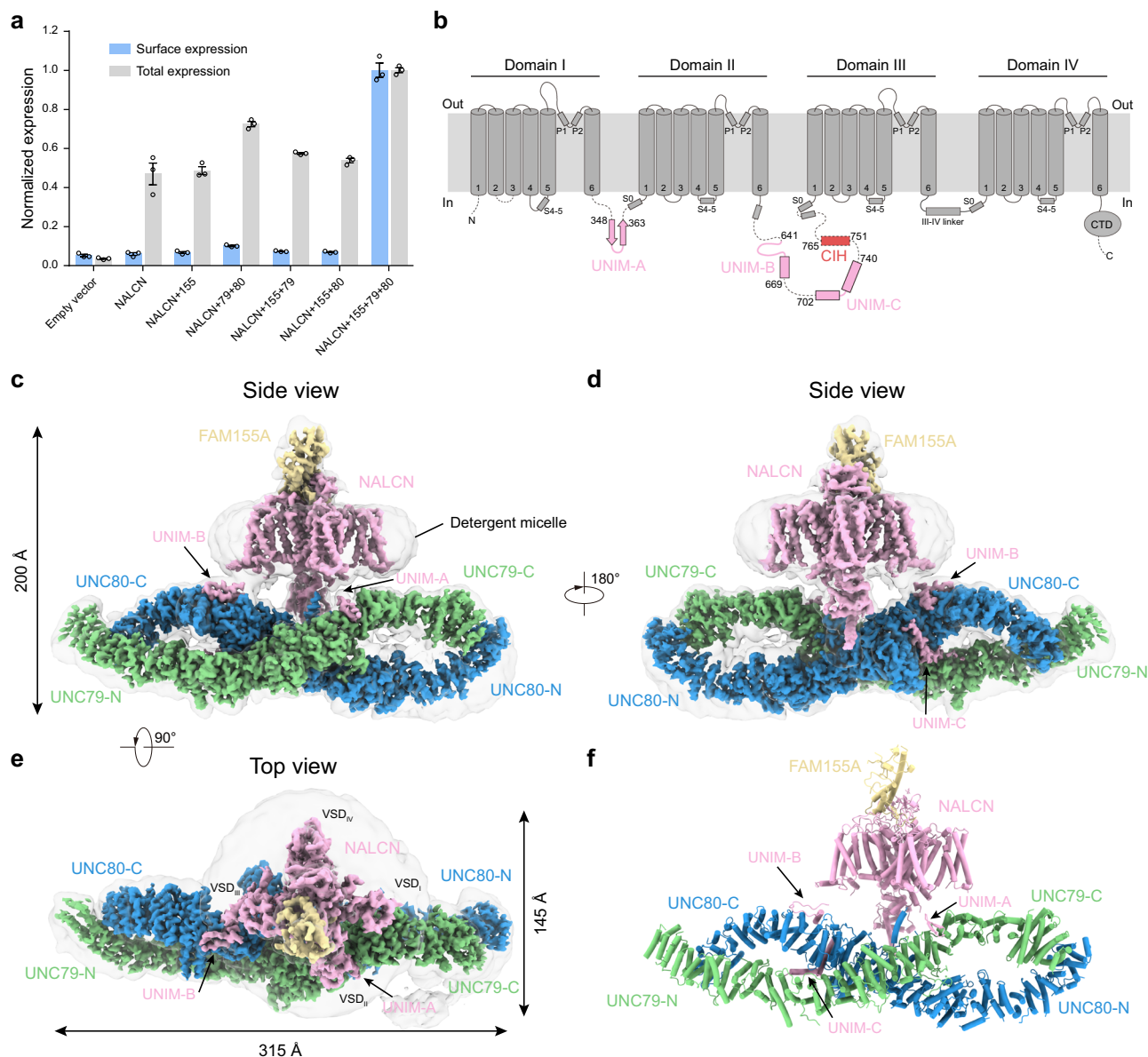


Fig. 1 Architecture of NALCN-FAM155A-UNC79-UNC80 quaternary complex. **a** The surface localization of the NALCN subunit in the presence or absence of FAM155A, UNC79, and UNC80. The signals of the 3×HA tag on the NALCN subunit in each combination were normalized to that of co-expression of NALCN, FAM155A, UNC79, and UNC80. Data were presented as mean ± SEM, *n* = 3 biologically independent samples. Source data are provided as a Source Data file. **b** Topology of the NALCN subunit. The UNC-interacting motifs (UNIM) located on intracellular loops of NALCN are shown in pink. The CTD-Interacting Helix (CIH) is shown in red. **c** The side view of cryo-EM map of NALCN-FAM155A-UNC79-UNC80 quaternary complex. NALCN, FAM155A, UNC79, and UNC80 are colored in pink, yellow, green, and blue, respectively. The detergent micelle and unresolved flexible region are shown in gray and in semi-transparency. **d** A 180° rotated side view of **c**. **e** A 90° rotated top view of **c**. **f** The atomic model of NALCN-FAM155A-UNC79-UNC80 quaternary complex. Each subunit is colored the same as in **c**.

blocks for UNC79 and UNC80 (Fig. 2a–d). We did not find any transmembrane helices of UNC79 or UNC80 in our cryo-EM density map. Although there is little sequence homology between UNC79 and UNC80, they share an overall wave-shaped structure formed by supercoiled helices (Fig. 2a–d). UNC79 and UNC80 interact in a head-to-tail fashion to form a plier-shape complex, akin to the infinity symbol “∞” (Fig. 2a–d). We divided the structures of UNC79 and UNC80 into five large consecutive functional domains: N-terminal UNC-heterodimerization domain (UHD-N), UNC connecting domain 1 (UCD1), middle UNC-heterodimerization domain (UHD-M), UNC connecting domain 2 (UCD2), and C-terminal UNC-heterodimerization domain (UHD-C) (Fig. 2a). UNC79 and UNC80 interact through

three regions: head, joint, and tail (Fig. 2b and Supplementary Fig. 6). The head region is formed by 79-UHD-N and 80-UHD-C, in which α5-α13 of UNC79 interact with α71-α76 of UNC80 (Fig. 2b–d and Supplementary Fig. 6b). The central joint region is formed by extensive interactions between the 79-UHD-M (α26-α49) and 80-UHD-M (α24-56) with an interface of 4270 Å² area (Fig. 2b–d and Supplementary Fig. 6c–g). The tail region is formed by 79-UHD-C and 80-UHD-N, in which α66-α71 of UNC79 interact with α1-α8 of UNC80 (Fig. 2b–d and Supplementary Fig. 6h).

Besides the HEAT and ARM repeats, there are also other recognizable structural modules present in the structures of UNC79 and UNC80. A ubiquitin-like domain (ULD) between

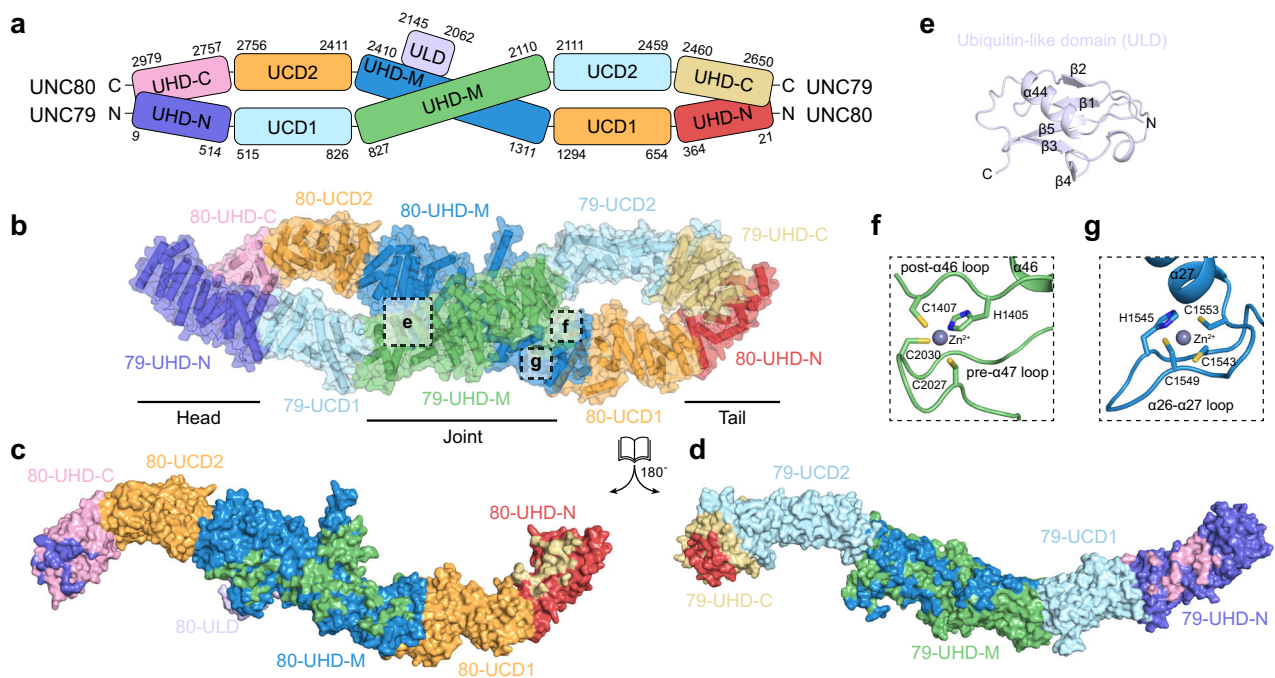


Fig. 2 Structure of UNC79-UNC80 heterodimer. **a** Cartoon representation of the domain organizations of UNC79 and UNC80. N-terminal UNC-heterodimerization domain (UHD-N), UNC connecting domain 1 (UCD1), middle UNC-heterodimerization domain (UHD-M), UNC connecting domain 2 (UCD2), and C-terminal UNC-heterodimerization domain (UHD-C). **b** Structure of UNC79-UNC80 heterodimer colored according to domain organization shown in **(a)**. The helices are shown as cylinders. **c, d** The open-book view of UNC79 and UNC80 shows their interaction interface. UNC79 and UNC80 are shown in surface representation and colored according to domain organization in **(a)**. Interaction interfaces on each domain are stained by the colors of their interaction partners. **e** The structure of ubiquitin-like domain (ULD) of UNC80 boxed in **(b)**. **f** The structure of the zinc finger domain of UNC79 boxed in **(b)**. **g** The structure of the zinc finger domain of UNC80 boxed in **(b)**.

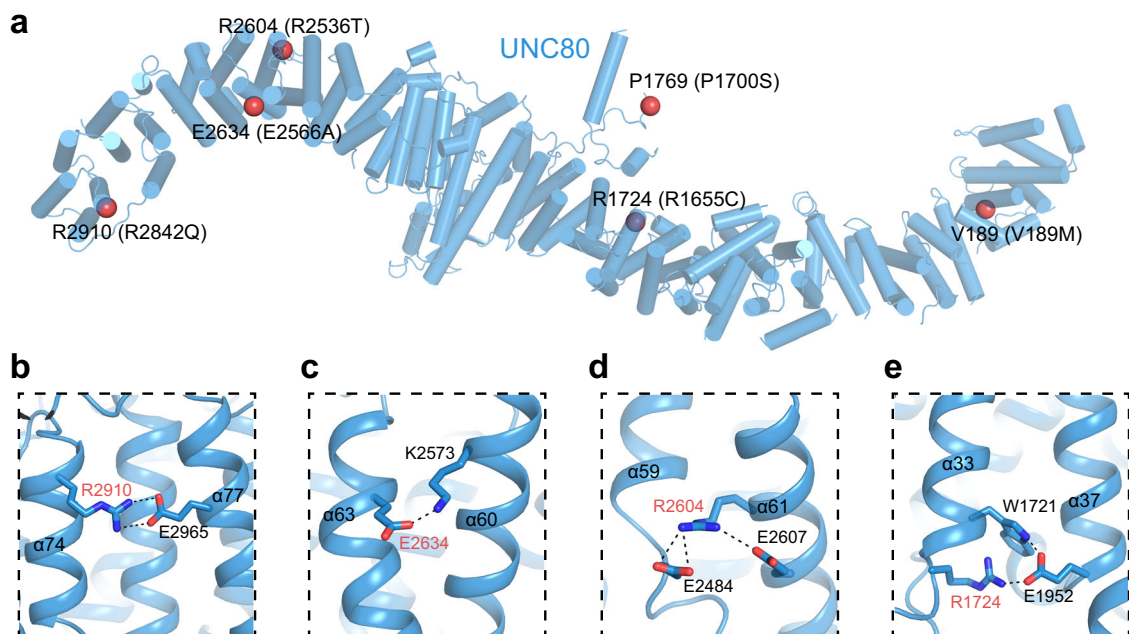


Fig. 3 Structural mapping of disease-causing mutations in UNC80. **a** Cartoon representation of UNC80. Helices are shown as cylinders. The C α atoms of disease-causing residues (corresponding mutations in humans are indicated in parenthesis) are shown as red spheres. **b-e** Close-up view of disease-causing residue (marked with red) and its interacting residues.

α43 and α45 of UNC80 protrudes out of 80-UHD-M (Fig. 2e). We observed one C3H-type zinc finger between α26 and α27 of 80-UHD-M (Fig. 2f), and another C3H-type zinc finger between α46 and α47 of 79-UHD-M (Fig. 2g). These structural modules are located on the surface of the UNC79-UNC80 heterodimer.

We further mapped the genetic mutations of UNC80 found in human patients onto the structure of rat UNC80^{13,23–26} (Fig. 3a). We found the majority of them are involved in intra-subunit interactions within UNC80. R2910 (R2842Q in human patients) on α74 interacts with E2965 on α77 (Fig. 3b); E2634 (E2566A in

human patients) interacts with K2573 on $\alpha 60$ (Fig. 3c); R2604 (R2536T in human patients) on $\alpha 61$ interacts with E2607 on $\alpha 61$ and E2484 close to $\alpha 59$ (Fig. 3d); R1724 (R1655C in human patients) on $\alpha 33$ interacts with E1952 on $\alpha 37$ (Fig. 3e). The disease-causing charge-neutralization mutations might abolish the electrostatic interactions within the UNC80 subunit and affect protein folding or overall conformation of UNC80 to impair its function, leading to human diseases.

Interactions between NALCN and UNC79-UNC80 heterodimer. NALCN interacts with UNC79-UNC80 heterodimer through three cytosolic UNC-interacting motifs (UNIM-A, B, C), which all are on loop regions of NALCN (Fig. 1b). UNIM-A (residues 348–363) locates on the D_{I-II} linker of NALCN and both UNIM-B (residues 641–669) and UNIM-C (residues 702–740) reside on the D_{II-III} linker (Fig. 1b). All of these UNIMs were not resolved in previous structures of the NALCN-FAM155 subcomplex, probably due to their high flexibilities in the absence of UNC79 and UNC80, which are their interaction partners. The location of UNIMs on the cytosolic loops of NALCN is consistent with the flexible tethering of the NALCN-FAM155A subcomplex with the UNC79-UNC80 heterodimer, evidenced by the relative motion between them observed in the cryo-EM analysis (Supplementary Movie 1).

UNIM-A has a short β hairpin structure which is inserted into a hydrophobic crevice formed between $\alpha 48$ – $\alpha 50$ of UNC79 (Fig. 4a). In detail, F351, W359, and L361 of UNIM-A make hydrophobic interactions with A2061, L2064, L2065, and M2068 on 79-UHD-M and I2113, L2117 on 79-UCD2 (Fig. 4a). To validate the structural observation biochemically, we used co-immunoprecipitation experiments to detect the interaction between GST-tagged UNIM-A and UNC79-UNC80 heterodimer (Fig. 4b). We found that UNIM-A could be co-immunoprecipitated by UNC79-UNC80 heterodimer (Fig. 4b). When we mutated the crucial hydrophobic residues on UNIM-A of NALCN (F351, W359, and L361) into alanines (UNIM-3A), such interaction was abolished (Fig. 4b).

UNIM-B shows a loop-like structure followed by a short helix. UNIM-B interacts with 80-UHD-M and 80-UCD2 (Fig. 4c). Hydrophobic residues on the loop, including V644, I646, L649, P650, F653, P656, and I658, pack onto a hydrophobic patch on the surface of UNC80, making hydrophobic interactions with L2417, V2419, V2421, and Y2424 on $\alpha 57$, and A2478 and Y2481 on $\alpha 59$ (Fig. 4c). The F662, M663, F666, and I667 on the helix of UNIM-B are inserted into a hydrophobic groove formed by

L2295 on $\alpha 52$, L2339, A2343 on $\alpha 55$, V2421, Y2424, A2425 on $\alpha 57$, and M2434 on $\alpha 58$ of UNC80 (Fig. 4c). Mutations of I658A, F662A, M663A, F666A, and I667A on NALCN (UNIM-B-5A) abolished the interaction between UNIM-B and UNC79-UNC80 heterodimer, evidenced by the co-immunoprecipitation experiment (Fig. 4d).

UNIM-C folds into an L-shape structure with two connecting helices (Fig. 4e). The first helix lies on the interface between 79-UHD-M and 80-UHD-M and the second helix is sandwiched between $\alpha 47$ and $\alpha 50$ of 80-UHD-M (Fig. 4e). R717 of UNIM-C makes electrostatic interactions with D917 of 79-UHD-M and E2270 of 80-UHD-M (Fig. 4e). K722 of UNIM-C makes polar interactions with Y2312 and the main-chain carbonyl group of L2267 of 80-UHD-M (Fig. 4e). V726, I729, and L730 of UNIM-C make hydrophobic interactions with I2206, F2210, I2266, and L2267 of 80-UHD-M (Fig. 4e). R737 makes hydrogen bonding with the main-chain carbonyl group of L2196 and L2198 of 80-UHD-M (Fig. 4e). Mutations of R717A, K722A, V726A, I729A, and L730A on NALCN (UNIM-C-5A) diminished the binding of UNIM-C to UNC79-UNC80 (Fig. 4d).

Mechanism of NALCN channel regulation by UNC79-UNC80.

Our structure suggests that the UNC79-UNC80 heterodimer regulates the NALCN channel through physical interactions with UNIMs of NALCN. In order to study the functional roles of these three identified interactions, we disrupted them individually by making the aforementioned mutations on UNIMs and recorded the NALCN currents of the mutants. We found mutations of UNIM-A (UNIM-A-3A) and UNIM-B (UNIM-B-5A) diminished the whole-cell currents of NALCN (Fig. 5a, b). The reduction of currents correlates with the reduced surface localization of NALCN (Fig. 5c). Therefore, we speculate that there are cytoplasmic retention signals on cytosolic regions of NALCN, and the binding of UNIM-A and UNIM-B onto the UNC79-UNC80 heterodimer masks such signals to facilitate the surface localization of the NALCN channel. This is akin to the K_{ATP} channel, in which the SUR subunits mask the ER retention signal of Kir6 subunits to promote the surface localization of the fully assembled K_{ATP} channel²⁷.

In contrast, the UNIM-C-5A mutant retains both robust whole-cell currents and surface localization compared to the wild-type channel (Fig. 5c, d). However, the conductance versus voltage (G-V) curve of the UNIM-C-5A mutant shifts to the positive potential compared with the wild-type channel (Fig. 5e),

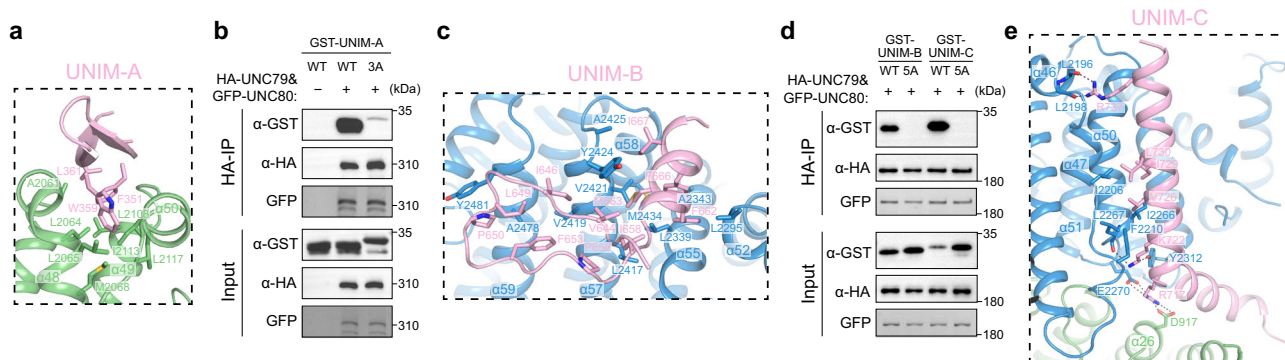


Fig. 4 Interaction between NALCN and UNC79-UNC80 heterodimer. **a** The interaction between UNIM-A in pink and UNC79 in green. Interacting residues are shown as sticks. **b** Co-immunoprecipitation between purified HA-UNC79-GFP-UNC80 heterodimer and GST-UNIM-A or its mutants UNIM-A-3A. The experiments were repeated independently three times with similar results. The original blots were provided as a Source Data file. **c** The interaction between UNC-interacting motif B (UNIM-B) in pink and UNC80 in blue. **d** Co-immunoprecipitation between HA-UNC79-GFP-UNC80 heterodimer and GST-UNIM-B, GST-UNIM-C, or their mutants UNIM-B-5A and UNIM-C-5A. The experiments were repeated independently three times with similar results. The original blots were provided as a Source Data file. **e** The interaction between UNC-interacting motif C (UNIM-C) in pink and UNC80 in blue.

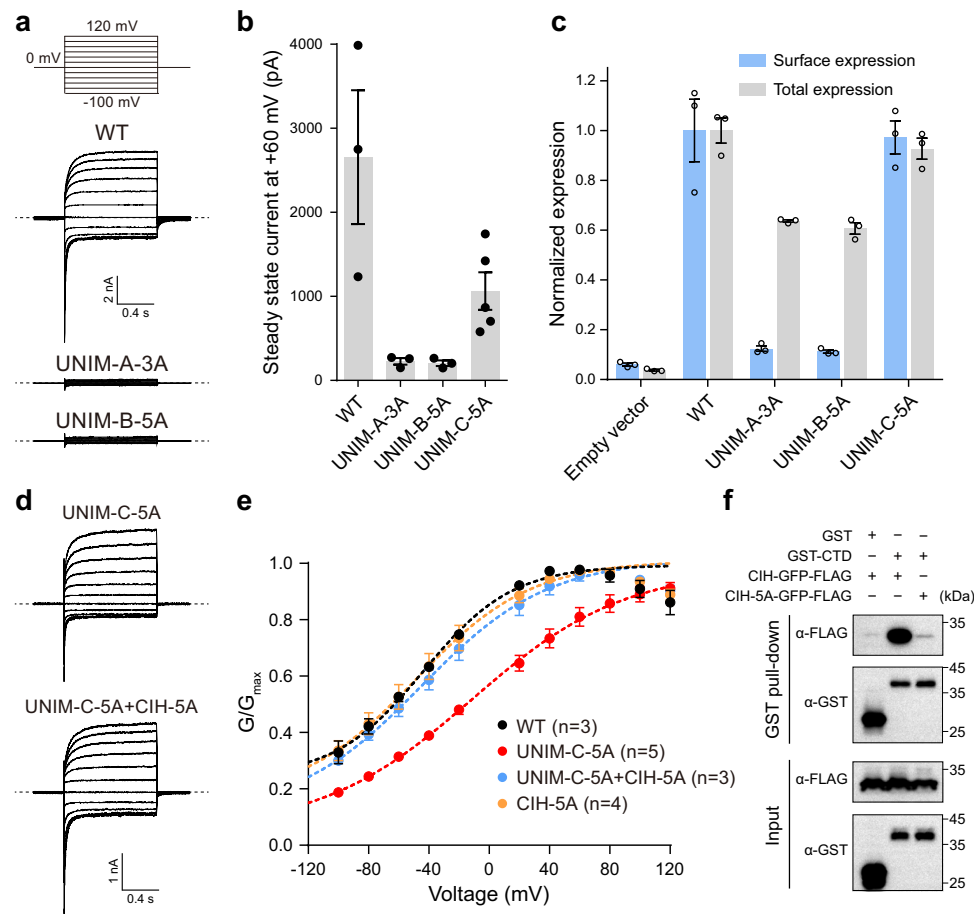


Fig. 5 Mechanism of NALCN activation by UNC79-UNC80 heterodimer. a The whole-cell voltage step protocol and representative whole-cell current traces of wild-type NALCN, UNIM-A-3A, or UNIM-B-5A mutants in the presence of FAM155A, UNC79, and UNC80. Dashed lines indicate the position of 0 nA. The experiments were repeated independently three times with similar results. **b** Whole-cell steady-state currents of wild-type NALCN, UNIM-A-3A, UNIM-B-5A, or UNIM-C-5A mutants in the presence of FAM155A, UNC79, and UNC80 at +60 mV. Data were presented as mean \pm SEM, $n = 3$ for WT, UNIM-A-3A, and UNIM-B-5A, $n = 5$ for UNIM-C-5A, biologically independent cells. Source data are provided as a Source Data file. **c** The normalized surface localization of the NALCN subunit and its mutants in the presence of FAM155A, UNC79, and UNC80. Data were presented as mean \pm SEM, $n = 3$ biologically independent samples. Source data are provided as a Source Data file. **d** Representative whole-cell current traces of UNIM-C-5A and UNIM-C-5A + CIH-5A mutants of NALCN in the presence of FAM155A, UNC79, and UNC80. The whole-cell voltage step protocol was the same as in **a**. Dashed lines indicate the position of 0 nA. The experiments were repeated independently at least three times with similar results. **e** Conductance versus voltage (G - V) curve of wild-type NALCN and its mutants in the presence of FAM155A, UNC79, and UNC80. The conductance at each voltage step was normalized to the maximum conductance obtained by fitting the data into the Boltzmann equation. Data were presented as mean \pm SEM, $n \geq 3$ biologically independent cells. Source data are provided as a Source Data file. **f** The GST pull-down assay of interactions between NALCN CTD and CIH-GFP or its mutant CIH-5A. The experiments were repeated independently three times with similar results. The original blots are provided as a Source Data file.

suggesting that the UNIM-C-5A mutation inhibits the opening of the NALCN. Close inspection of the cryo-EM map showed that the CIH density was missing in the NALCN-FAM155A-UNC79-UNC80 quaternary complex (Supplementary Fig. 7a). Both UNIM-C (702-740) and CIH (751-765) are on the D_{II-III} linker of NALCN and there are only ten amino acids between UNIM-C and CIH. If we modeled the CIH in its binding site of NALCN CTD of the quaternary complex, we found the linear distance between the termini of UNIM-C and CIH is about 60 Å (Supplementary Fig. 7b), which is much longer than the distance that ten amino acids could extend to, even in their fully extended conformation. Moreover, there are several structural elements between the CIH-binding site on NALCN and the UNIM-C binding site on UNC79-UNC80 heterodimer, including S6_{II}-UNIM-B linker, CIH-VSD_{III} linker, C-terminal flexible region of NALCN, and several flexible linkers of UNC79 and UNC80, all of which might generate putative steric hindrance. Therefore, our structural observation and modeling study suggest that the

binding of UNIM-C of NALCN D_{II-III} linker to the UNC79-UNC80 heterodimer in the quaternary complex would prevent the binding of its neighboring CIH in the CIH-binding pocket of NALCN CTD, likely through spacial constrain, and UNIM-C-5A mutations would disrupt the binding of UNIM-C to UNC79-UNC80 and would release the constrain of UNIM-C on CIH to allow it to re-bind to NALCN CTD. The rightward shift of the G - V curve of the UNIM-C-5A mutant indicates that the binding of CIH in CTD inhibits channel opening, probably by stabilizing the channel in a closed state. To further validate this model, we looked for the mutants on CIH which could disrupt the interaction between CIH and CTD. Guided by our previous high-resolution structure of NALCN-FAM155A subcomplex¹⁵, we found that the combination of I753A, L754A, R761A, R764A, and R765A mutations (CIH-5A) is sufficient to disrupt such interaction, shown by GST pull-down assay (Fig. 5f). We hypothesize that the CIH-5A mutation might release the self-inhibition of NALCN. Indeed, we found that additional CIH-5A

mutation on the background of UNIM-C-5A mutant shifts the G-V curve of UNIM-C-5A back to the level similar to the wild-type channel, while CIH-5A itself has no effect on the gating of NALCN (Fig. 5e). These results are in agreement with our mechanistic model.

Discussion

Notably, during the submission process of this manuscript, another group published a cryo-EM structure of the human NALCN-FAM155A-UNC79-UNC80 complex²⁸. Their structures of NALCN-FAM155A subcomplex and UNC79-UNC80 heterodimer are highly similar to ours (Supplementary Fig. 8b, c). But the orientations between NALCN-FAM155A subcomplex and UNC79-UNC80 heterodimer show some differences, likely due to the conformational heterogeneity or different cryo-EM sample preparation procedures (Supplementary Fig. 8d). In addition to the over-expressed NALCN, FAM155A, UNC79, and UNC80 proteins, they identified an endogenous calmodulin protein that is bound on the C-terminal helix of NALCN²⁸. We also observed extra densities at similar positions not only in our current cryo-EM maps of the quaternary complex but also in our previously published NALCN-FAM155A subcomplex¹⁵ (Supplementary Fig. 8e, f). However, the poor local map qualities of these densities preclude the confident assignment of their identities.

In summary, the near-atomic resolution structure of the NALCN-FAM155A-UNC79-UNC80 complex presented here shows the architecture of the functional mammalian NALCN channel complex, reveals the structure of the UNC79-UNC80 heterodimer, and depicts the detailed interactions between UNC79 and UNC80. More importantly, our structure and accompanying functional studies uncover the activation mechanism of the NALCN channel by UNC79-UNC80 heterodimer, not only through promoting the surface localization of NALCN but also through modulating the gating of NALCN (Fig. 6). Our work provides a solid framework for a further mechanistic understanding of the NALCN complex and to target the NALCN channel for therapeutic intervention.

Methods

Cell culture. Sf9 insect cells (Thermo Fisher Scientific, Waltham, MA, USA) were cultured in SIM SF (Sino Biological, China) at 27 °C. FreeStyle 293 F suspension cells (Thermo Fisher Scientific) were cultured in FreeStyle 293 medium (Thermo Fisher Scientific) supplemented with 1% fetal bovine serum (FBS) at 37 °C with 6% CO₂ and 70% humidity. HEK293T (ATCC) were cultured in Dulbecco's Modified Eagle Medium (Gibco, Gaithersburg, MD USA) supplemented with 10% FBS at 37 °C with 5% CO₂. The cell lines were routinely checked to be negative for mycoplasma contamination but have not been authenticated.

Determination of the surface expression of the NALCN subunit. HEK293T cells were plated onto a poly-D-lysine treated 24-well plate (303002; Corning) and transfected with indicated plasmids (Figs. 1a, 5c, in a modified BacMam expression vector²⁹) at a ratio of 1:1.5:1.75:2 (FAM155A-3×FLAG:NALCN-1077-3×HA-GFP:UNC79-3×FLAG:UNC80-3×FLAG) using Lipofectamine 3000 (Thermo Fisher Scientific) and incubated for 40–48 h. When certain constructs were excluded from the transfection, an equal amount of empty vector was added. The cells were washed with PBS twice, fixed using 4% formaldehyde in PBS for 30 min, and washed with PBS twice again. Then the cells were blocked with 3% goat serum in PBS for 30 min and labeled with primary antibody [rabbit anti-HA (3724; CST, diluted 2500 times in blocking buffer)] for 1 h. After washing with PBS for three times, cells were incubated with horseradish-peroxidase (HRP) labeled goat anti-rabbit secondary antibody (31460; Thermo Fisher Scientific, the antibody was diluted 2,500 times in blocking buffer) for 30 min. After extensive washing, the cells were incubated with High-Sig ECL Western Blotting Substrate (Tanon) for 2 min, and chemiluminescence signals were measured with an Infinite M Plex plate reader (Tecan). The signals represent the surface expression of the NALCN subunit. Then the cells were permeabilized by incubating in PBS with 0.1% TX-100 for 30 min. The cells were subsequently blocked, labeled with primary and secondary antibodies, and detected by ECL chemiluminescence as described above. The chemiluminescence signals of permeabilized cells represent the total expression of NALCN.

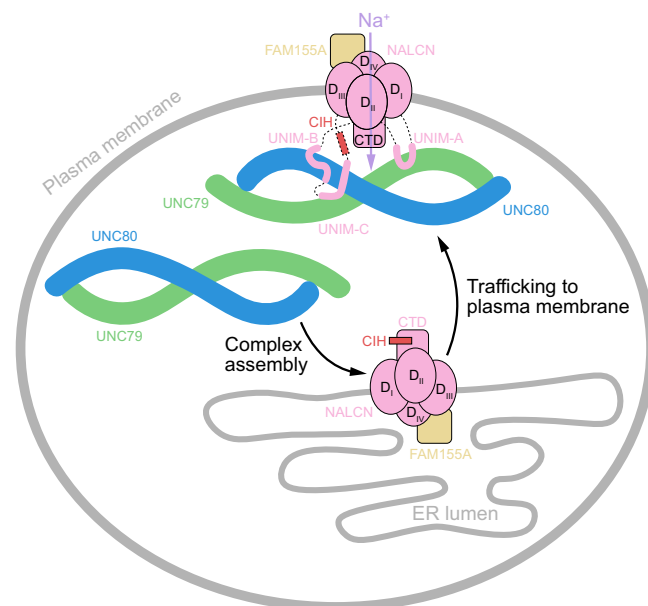


Fig. 6 Mechanistic model of NALCN-FAM155A-UNC79-UNC80 channel complex. NALCN, FAM155A, UNC79, and UNC80 are shown as cartoons and colored the same as Fig. 1c. Initially, the NALCN-FAM155A subcomplex is assembled in an intracellular compartment. Subsequently, the UNC79-UNC80 heterodimer binds to the UNIM-A, B, and C of the NALCN-FAM155A subcomplex to activate the channel. The binding of UNC79-UNC80 with UNIM-A and UNIM-B promotes plasma localization of the NALCN complex. Binding of UNC79-UNC80 with UNIM-C releases the auto-inhibition of NALCN by CIH.

Fluorescence-detection size-exclusion chromatography (FSEC). Purified protein or cell lysates were injected onto a Superose 6 increase 5/150 column (GE Healthcare), running in a buffer containing 20 mM Tris (pH 7.5), 150 mM NaCl, 0.5 mM *n*-dodecyl β -D-maltoside (DDM, Anatrace), and detected by a fluorescence detector (Shimadzu, excitation 488 nm and emission 520 nm for GFP signal) at room temperature.

Electrophysiology. HEK293T cells were co-transfected with constructs containing rNALCN-GFP, mFAM155A-FLAG, mScarlet-mUNC80, and HA-mUNC79 plasmids or their various mutants (in a modified BacMam expression vector²⁹) at a ratio of 2:1:1:1 using Lipofectamine 3000 (Thermo Fisher Scientific) and incubated for 24 h before recording. Patch electrodes were pulled with a horizontal micro-electrode puller (P-1000, Sutter Instrument Co, USA) to a resistance of 1.7–2.5 M Ω . Whole-cell patch clamps were performed using an Axon-patch 200B amplifier (Axon Instruments, USA), and data were collected with pClamp 10 software (Axon Instruments, USA) and an Axon Digidata 1550B digitizer (Axon Instruments, USA). Pipette solution containing (mM): 10 HEPES (pH 7.2, NaOH), 136 NaCl, 10 NaF, 5 EGTA, 2 Na₂ATP and bath solution containing (mM): 10 HEPES (pH 7.4, NaOH), 150 NaCl, 30 glucose. At the end of each experiment, the bath solution was exchanged to 10 mM HEPES (pH 7.4, HCl), 150 mM NMDG, and 30 mM glucose by a local perfusion system (MPS-2, InBio) to exclude the loosely sealed patch (cells with current < -100 pA at -100 mV was discarded). Serial resistance was compensated by at least 75%. The steady-state currents were used to generate G/G_{max} versus V curves ($G = I/V$). The Boltzmann equation was used to fit the G-V curve in GraphPad Prism 6. Signals were acquired at 5 kHz and low-pass filtered at 1 kHz. The data were processed using Clampfit, Microsoft Excel, and GraphPad Prism 6.

Protein expression and purification. The cDNAs of rat NALCN, mouse FAM155A, mouse UNC79, and mouse UNC80 were cloned into a modified BacMam expression vector²⁹ with a C-terminal GFP-strep-FLAG tag, a FLAG tag, N-terminal HA tag, and NbGFP-strep-FLAG tag, respectively. The baculoviruses were produced using the Bac-to-Bac system and amplified in Sf9 cells. We expressed NALCN-FAM155A subcomplex and UNC79-UNC80 heterodimer separately. For protein expression, FreeStyle 293 F cells cultured in FreeStyle 293 medium at a density of 2.5×10^6 ml⁻¹ were infected with 6% volume of NALCN P2 virus and 4% volume of FAM155A P2 virus or 6% volume of UNC79 P2 virus and 4% volume of UNC80 P2 virus. About 10 mM sodium butyrate was added to the culture 12 h post-infection and transferred to a 30 °C incubator for another 48 h (NALCN-FAM155A) or 60 h (UNC79-UNC80) before harvesting. Cells were

collected by centrifugation at $3990 \times g$ (JLA-8.1000, Beckman) for 10 min, and washed with 20 mM Tris (pH 7.5), 150 mM NaCl, 2 $\mu\text{g}/\text{ml}$ aprotinin, 2 $\mu\text{g}/\text{ml}$ pepstatin, and 2 $\mu\text{g}/\text{ml}$ leupeptin, flash frozen and storage at -80°C .

For each batch of protein purification, cell pellets corresponding to 0.6 liter culture of NALCN-FAM155A or UNC79-UNC80 was thawed and extracted with 42 or 21 ml lysis buffer containing 50 mM HEPES (pH 8.0), 150 mM NaCl, 2 $\mu\text{g}/\text{ml}$ aprotinin, 2 $\mu\text{g}/\text{ml}$ pepstatin, 2 $\mu\text{g}/\text{ml}$ leupeptin, 10% (v/v) glycerol, 1 mM phenylmethanesulfonyl fluoride (PMSF), 2 mM MgCl_2 , 0.7 $\mu\text{g}/\text{ml}$ benzamide, 1 mg/ml iodoacetamide and 1% (w/v) glyco-diosgenin (GDN, Anatrace) at 4°C for 1 h, respectively. The lysates were then mixed and incubated for 30 min and centrifuged at $40,000 \times g$ (JA-25.5, Beckman) for 40 min at 4°C . The supernatant was incubated with 1 ml Anti-FLAG Affinity Beads (Smart-Lifesciences) for 90 min at 4°C and washed with 5 ml W buffer (20 mM HEPES (pH 8.0), 150 mM NaCl, 10% glycerol, 2 $\mu\text{g}/\text{ml}$ aprotinin, 2 $\mu\text{g}/\text{ml}$ pepstatin, 2 $\mu\text{g}/\text{ml}$ leupeptin, and 0.02% GDN) for four times. The target protein was eluted with 1 ml W buffer plus 200 $\mu\text{g}/\text{ml}$ 3 \times FLAG peptides (Smart-Lifesciences) and 30 mM HEPES (pH 8.0) five times. The eluate was loaded onto 2 ml Streptactin Beads 4FF (Smart-Lifesciences) column and washed with 45 ml W buffer plus 2 mM ATP and 10 mM MgCl_2 , and washed with 20 mM HEPES (pH 8.0), 150 mM NaCl, 10% glycerol and 0.02% GDN for 20 ml. The target protein was eluted by 25 mM HEPES (pH 8.5), 150 mM NaCl, 10% glycerol, 0.02% GDN and 5 mM desthiobiotin (IBA). Eluted protein was crosslinked with 0.04% glutaraldehyde (EM-grade, Sigma) on ice for 25 min, and stopped with 50 mM Tris-HCl (pH 7.5) on ice for 15 min. Crosslinked protein was concentrated using a 100-kDa cut-off concentrator (Millipore) and further purified by Superose 6 increase (GE Healthcare) running in a buffer containing 20 mM Tris (pH 7.5), 150 mM NaCl and 0.006% GDN. Fractions corresponding to NALCN-FAM155A-UNC79-UNC80 complex were pooled and concentrated to $A_{280} = 0.38$ for cryo-EM sample preparation.

Cryo-EM sample preparation and data collection. Holey carbon grids (Quantifoil Au 300 mesh, R 0.6/1) coated with homemade ultrathin continuous carbon were glow-discharged by plasma cleaner (Harrick, PDC-32G) for 30 s with the “Low” setting. Aliquots of 3 μl concentrated protein sample were applied on glow-discharged grids and the grids were blotted for 2 s before being plunged into liquid ethane using Vitrobot Mark IV (Thermo Fisher Scientific). Cryo-grids were firstly screened on a Talos Arctica electron microscope (Thermo Fisher Scientific) operating at 200 kV with a K2 Summit direct electron camera (Gatan). The screened grids were subsequently transferred to a Titan Krios electron microscope (Thermo Fisher Scientific) operating at 300 kV with a K2 Summit direct electron camera and a GIF Quantum energy filter set to a slit width of 20 eV. Images were automatically collected using SerialEM in super-resolution mode at a nominal magnification of 105,000 \times , corresponding to a calibrated super-resolution pixel size of 0.662 \AA with a preset defocus range from -1.5 to $-1.8 \mu\text{m}$. Each image was acquired as a 10 s movie stack of 40 frames with a dose rate of $5 \text{e}^- \text{\AA}^{-2} \text{s}^{-1}$, resulting in a total dose of about $50 \text{e}^- \text{\AA}^{-2}$.

Cryo-EM image analysis. The image processing workflow is illustrated in Supplementary Fig. 2c. A total of 6714 super-resolution movie stacks were collected. Motion-correction, two-fold binning to a pixel size of 1.324 \AA , and dose weighting were performed using MotionCor2³⁰. Contrast transfer function (CTF) parameters were estimated with Gctf³¹. Micrographs with ice or ethane contamination and empty carbon were removed manually. A total of 2,742,149 particles were auto-picked using Gautomatch from 6156 micrographs. All subsequent classification and reconstruction were performed in Relion 3.1³² unless otherwise stated. Two rounds of reference-free 2D classification were performed to remove contaminants, yielding 797,032 particles. The particles were subjected to 30 iterations $K = 1$ global search 3D classification with an angular sampling step of 7.5° to determine the initial alignment parameters using the initial model generated from cryoSPARC³³. For each of the last five iterations of the global search, a $K = 4$ multi-reference (resolution gradient) local angular search 3D classification with the mask of UNC79-UNC80 was performed with an angular sampling step of 3.75° and search range of 30° . The classes that showed obvious secondary structure features were selected and combined. Duplicated particles were removed, yielding 567,778 particles in total. These particles were subjected to additional six rounds of multi-reference local angular search 3D classification with the mask of UNC79-UNC80 using resolution gradient references or good and phase randomized references, yielding 202,781 particles. These particles were subsequently subjected to local NU-refinement in cryoSPARC with the mask of UNC79-UNC80³⁴, which resulted in a map with a resolution of 3.3 \AA . To further improve the resolution, seed-facilitated 3D classification was performed³⁵. The CTF parameters were re-estimated with Patch CTF in cryoSPARC. 486,791 particles were selected after two rounds of seed-facilitated 3D classification using good and biased references or references with resolution gradients in cryoSPARC. These particles were subjected to reference-free 2D classification, yielding 430,068 particles. The particles were subjected to global and local search 3D classification to determine the correct alignment parameters, yielding 336,476 particles. In further cleaning up the dataset, no alignment 3D classification was performed with the mask of the UNC79-UNC80 middle region. Particles with the best features were selected, yielding 275,170 particles. These particles were subjected to local NU-refinement in cryoSPARC with the mask of UNC79-UNC80 or whole complex, which resulted in maps with resolutions of 3.1

and 3.2 \AA , respectively. We applied different local masks of UNC79-UNC80 fragments to improve the local map quality, yielding four overlapping focus-refined maps with resolutions of 2.9–3.4 \AA . Due to the relative motions between NALCN-FAM155A and UNC79-UNC80, we performed particle subtraction to remove signals of UNC79-UNC80 to improve the alignment of the NALCN-FAM155A subcomplex. After three rounds of local search 3D classification using subtracted particles, 68,126 particles were selected. These particles were subjected to local NU-refinement in cryoSPARC with the mask of NALCN-FAM155A, yielding a map with a resolution of 3.7 \AA . These subtracted particles were re-extracted on original micrographs and analyzed by multi-body refinement with masks of NALCN-FAM155A and UNC79-UNC80²⁰. We also performed a 3D variability analysis after consensus refinement in cryoSPARC²¹. The focus-refined maps were combined using *vop maximum* command in UCSF Chimera to generate the composite map for model building and interpretation.

All of the resolution estimations were based on a Fourier shell correlation (FSC) of 0.143 cutoff after correction of the masking effect. B-factor used for map sharpening was automatically determined by NU-refinement in cryoSPARC. The local resolution was estimated with Relion 3.1 with half maps output from cryoSPARC.

Model building. The model of NALCN-FAM155A (PDB ID: 7CU3) was docked into the electron density map using UCSF Chimera³⁶ and manually adjusted using Coot³⁷. The models of the UNC79-UNC80 joint region were built manually using Coot. The models of UNC79-UNC80 head and tail regions were predicted by AlphaFold2²², docked into a cryo-EM map, and manually adjusted using Coot. The initial models of UNIMs were traced by DeepTracer³⁸ according to the cryo-EM maps and protein sequences and re-built manually using Coot. Model refinement was performed using phenix.real_space_refine in PHENIX³⁹. Images were produced using Pymol, UCSF Chimera³⁶, and ChimeraX⁴⁰. Sequence alignment was performed with ClustalX2⁴¹ and illustrated by ESPript 3.0⁴².

Co-immunoprecipitation. For co-immunoprecipitation between UNIM-A and UNC79-UNC80 (Fig. 4b), a fragment of UNIM-A WT or 3 A mutant was cloned into a pGEX-6P-1 vector. GST-UNIM-A WT or 3 A was over-expressed in *E. coli* NiCo21 (DE3) induced with 1 mM isopropyl- β -D-thiogalactoside (IPTG) when the cell density reached $\text{OD}_{600} = 0.6$ for 4 h at 37°C . The cells were collected and sonicated in lysis buffer containing 50 mM Tris (pH 7.5), 150 mM NaCl, 2 $\mu\text{g}/\text{ml}$ aprotinin, 2 $\mu\text{g}/\text{ml}$ pepstatin, 2 $\mu\text{g}/\text{ml}$ leupeptin, and 1 mM PMSF. Then the cell debris was removed by centrifugation at $30,966 \times g$ (JA-25.50, Beckman) for 30 min. The supernatants were loaded onto Glutathione Sepharose 4B and washed with 20 mM Tris (pH 7.5), 150 mM NaCl and eluted with 50 mM Tris (pH 8.0), 50 mM NaCl and 10 mM reduced glutathione. GST eluates were further purified with an anion exchange column (HiTrap Q HP, GE Healthcare) and the peak fractions were pooled for co-immunoprecipitation experiments. To obtain the protein of UNC79-UNC80 heterodimer, we expressed and purified N-terminal HA-tagged UNC79 and GFP-strep tagged UNC80 by infecting FreeStyle 293 F cells with corresponding BacMam viruses. Protein was purified with Streptactin affinity beads as described in “Protein expression and purification” section. About 200 μl of purified GST-UNIM-A-WT/3 A ($A_{280} = 0.744$, diluted by 20 mM Tris (pH 7.5), 150 mM NaCl, 10% glycerol, 2 $\mu\text{g}/\text{ml}$ aprotinin, 2 $\mu\text{g}/\text{ml}$ pepstatin, 2 $\mu\text{g}/\text{ml}$ leupeptin and 0.006% GDN) was mixed with 100 μl purified HA-UNC79 and GFP-UNC80 heterodimer ($A_{280} = 0.138$ in Streptactin elution buffer, 20 μl of the mixture was saved as input) and incubated with Anti-HA Magnetic Beads (88836; Thermo Fisher Scientific) for 2 h at 4°C . The beads were washed with 20 mM Tris (pH 7.5), 80 mM NaCl, 2 $\mu\text{g}/\text{ml}$ aprotinin, 2 $\mu\text{g}/\text{ml}$ pepstatin, 2 $\mu\text{g}/\text{ml}$ leupeptin, 10% glycerol and 0.006% GDN five times, and eluted with 30 μl SDS-PAGE loading buffer (without reducing agent).

For co-immunoprecipitation of UNIM-B/C and UNC79-UNC80 (Fig. 4d), cDNA of UNIM-B/C WT or 5 A mutant was cloned into a modified BacMam expression vector²⁹. FreeStyle 293 F cells cultured in FreeStyle 293 medium were transfected with indicated plasmids (Fig. 4d) at a ratio of 1:1:1 using PEI. 48 h post-transfection, 2 ml cells were collected and lysed using 300 μl 20 mM Tris (pH 7.5), 150 mM NaCl, 2 $\mu\text{g}/\text{ml}$ aprotinin, 2 $\mu\text{g}/\text{ml}$ pepstatin, 2 $\mu\text{g}/\text{ml}$ leupeptin, 1 mM PMSF, 20% glycerol and 0.5% GDN at 4°C for 30 min. After ultra-centrifugation at $100,000 \times g$ (TLA-55, Beckman) for 30 min, the supernatants (20 μl of lysate was saved as input) were mixed with Anti-HA Magnetic Beads (88836; Thermo Fisher Scientific) and incubated at 4°C for 2.5 h. Then the beads were washed with 20 mM Tris (pH 7.5), 150 mM NaCl, 2 $\mu\text{g}/\text{ml}$ aprotinin, 2 $\mu\text{g}/\text{ml}$ pepstatin, 2 $\mu\text{g}/\text{ml}$ leupeptin, 20% glycerol, and 0.006% GDN five times. Bound proteins were eluted with 30 μl SDS-PAGE loading buffer (without reducing agent).

Proteins of input and elution were separated with SDS-PAGE and transferred onto polyvinylidene difluoride (PVDF) membranes (GFP signal was detected by in-gel fluorescence). PVDF membranes were blocked using 5% nonfat milk in TBST [25 mM Tris (pH 7.4), 137 mM NaCl, 3 mM KCl and 0.1% Tween-20] for 1 h at room temperature and incubated with primary antibodies [mouse anti-GST (30901ES10; Yeasen Biotechnology) or rabbit anti-HA (3724; CST)], both of antibodies were diluted 5,000 times] overnight at 4°C . Then membranes were incubated with corresponding horseradish-peroxidase (HRP) labeled goat anti-mouse secondary antibody (31444; Thermo Fisher Scientific) or horseradish-peroxidase (HRP) labeled goat anti-rabbit secondary antibody (31460; Thermo

Fisher Scientific, both of antibodies were diluted 10,000 times) for 1 h at room temperature and developed using High-Sig ECL Western Blotting Substrate (Tanon).

GST pull-down assay. FreeStyle 293 F cells cultured in FreeStyle 293 medium were transfected with indicated plasmids (Fig. 5f) at a ratio of 1:1 using PEI. Forty-eight hours post-transfection, cells were collected and sonicated in a buffer containing 20 mM Tris (pH 7.5), 150 mM NaCl, 2 µg/ml aprotinin, 2 µg/ml pepstatin, 2 µg/ml leupeptin, 1 mM PMSF. After centrifugation at 16,162 × g for 20 min, the supernatants were mixed with Glutathione Sepharose 4B (GE Healthcare) and incubated at 4 °C for 1 h. Then the beads were washed with 20 mM Tris (pH 7.5) and 150 mM NaCl six times. Bound proteins were eluted with 50 mM Tris (pH 8.0), 150 mM NaCl, and 10 mM reduced glutathione.

For Western blot, proteins were separated with 10% SDS-PAGE and transferred onto PVDF membranes. Membranes were blocked using 5% nonfat milk in TBST for 1 h at room temperature and incubated with primary antibodies [mouse anti-GST (30901ES10; Yeasen Biotechnology) or mouse anti-FLAG (M20008M; Abmart), both antibodies were diluted 5000 times] overnight at 4 °C. Then membranes were incubated with horseradish-peroxidase (HRP) labeled goat anti-mouse secondary antibody (31444; Thermo Fisher Scientific, the antibody was diluted 10,000 times) for 1 h at room temperature and developed using High-Sig ECL Western Blotting Substrate (Tanon).

Quantification and statistical analysis. Global resolution estimations of cryo-EM density maps are based on the 0.143 Fourier Shell Correlation criterion⁴³. The local resolution was estimated using Relion 3.1 with half maps output from cryoSPARC. The number of independent experiments (*N*) and the relevant statistical parameters for each experiment (such as mean or standard error of the mean) are described in the figure legends. No statistical methods were used to pre-determine sample sizes.

Reporting summary. Further information on research design is available in the Nature Research Reporting Summary linked to this article.

Data availability

The data supporting the findings of this manuscript are available from the corresponding author upon reasonable request. The Cryo-EM map and atomic coordinate of the NALCN-FAM155A-UNC97B-UNC80 complex have been deposited in the EMDB and PDB under the ID codes EMD-32344 and 7W7G, respectively. EMDB entry EMD-30470 and PDB entries 7CU3 and 7SX3 used in this study were downloaded from EM Data Bank and Protein Data Bank, respectively. Source data are provided with this paper.

Received: 7 January 2022; Accepted: 27 April 2022;

Published online: 12 May 2022

References

- Chua, H. C., Wulf, M., Weidling, C., Rasmussen, L. P. & Pless, S. A. The NALCN channel complex is voltage sensitive and directly modulated by extracellular calcium. *Sci. Adv.* **6**, eaaz3154 (2020).
- Ren, D. Sodium leak channels in neuronal excitability and rhythmic behaviors. *Neuron* **72**, 899–911 (2011).
- Al-Sayed, M. D. et al. Mutations in NALCN cause an autosomal-recessive syndrome with severe hypotonia, speech impairment, and cognitive delay. *Am. J. Hum. Genet.* **93**, 721–726 (2013).
- Koroglu, C., Seven, M. & Tolun, A. Recessive truncating NALCN mutation in infantile neuroaxonal dystrophy with facial dysmorphism. *J. Med. Genet.* **50**, 515–520 (2013).
- Chong, J. X. et al. De novo mutations in NALCN cause a syndrome characterized by congenital contractures of the limbs and face, hypotonia, and developmental delay. *Am. J. Hum. Genet.* **96**, 462–473 (2015).
- Lu, B. et al. The neuronal channel NALCN contributes resting sodium permeability and is required for normal respiratory rhythm. *Cell* **129**, 371–383 (2007).
- Funato, H. et al. Forward-genetics analysis of sleep in randomly mutagenized mice. *Nature* **539**, 378–383 (2016).
- Stephens, R. F., Guan, W., Zhorov, B. S. & Spafford, J. D. Selectivity filters and cysteine-rich extracellular loops in voltage-gated sodium, calcium, and NALCN channels. *Front. Physiol.* **6**, 153 (2015).
- Xie, L. et al. NLF-1 delivers a sodium leak channel to regulate neuronal excitability and modulate rhythmic locomotion. *Neuron* **77**, 1069–1082 (2013).
- Humphrey, J. A. et al. A putative cation channel and its novel regulator: cross-species conservation of effects on general anesthesia. *Curr. Biol.* **17**, 624–629 (2007).
- Jospin, M. et al. UNC-80 and the NCA ion channels contribute to endocytosis defects in synaptojanin mutants. *Curr. Biol.* **17**, 1595–1600 (2007).
- Yeh, E. et al. A putative cation channel, NCA-1, and a novel protein, UNC-80, transmit neuronal activity in *C. elegans*. *PLoS Biol.* **6**, e55 (2008).
- Stray-Pedersen, A. et al. Biallelic Mutations in UNC80 Cause Persistent Hypotonia, Encephalopathy, Growth Retardation, and Severe Intellectual Disability. *Am. J. Hum. Genet.* **98**, 202–209 (2016).
- Lu, B. et al. Extracellular calcium controls background current and neuronal excitability via an UNC97B-UNC80-NALCN cation channel complex. *Neuron* **68**, 488–499 (2010).
- Kang, Y., Wu, J. X. & Chen, L. Structure of voltage-modulated sodium-selective NALCN-FAM155A channel complex. *Nat. Commun.* **11**, 6199 (2020).
- Kschonsak, M. et al. Structure of the human sodium leak channel NALCN. *Nature* <https://doi.org/10.1038/s41586-020-2570-8> (2020).
- Xie, J. et al. Structure of the human sodium leak channel NALCN in complex with FAM155A. *Nat. Commun.* **11**, 5831 (2020).
- Margeta-Mitrovic, M., Jan, Y. N. & Jan, L. Y. A trafficking checkpoint controls GABA(B) receptor heterodimerization. *Neuron* **27**, 97–106 (2000).
- Kirchhofer, A. et al. Modulation of protein properties in living cells using nanobodies. *Nat. Struct. Mol. Biol.* **17**, 133–138 (2010).
- Nakane, T., Kimanius, D., Lindahl, E. & Scheres, S. H. Characterisation of molecular motions in cryo-EM single-particle data by multi-body refinement in RELION. *Elife* <https://doi.org/10.7554/eLife.36861> (2018).
- Punjani, A. & Fleet, D. J. 3D variability analysis: resolving continuous flexibility and discrete heterogeneity from single particle cryo-EM. *J. Struct. Biol.* **213**, 107702 (2021).
- Jumper, J. et al. Highly accurate protein structure prediction with AlphaFold. *Nature* **596**, 583–589 (2021).
- Nair, P. et al. Contribution of next generation sequencing in pediatric practice in Lebanon. A Study on 213 cases. *Mol. Genet. Genom. Med.* **6**, 1041–1052 (2018).
- Shamseldin, H. E. et al. Mutations in UNC80, encoding part of the UNC97B-UNC80-NALCN channel complex, cause autosomal-recessive severe infantile encephalopathy. *Am. J. Hum. Genet.* **98**, 210–215 (2016).
- Obeid, T. et al. Identification of a novel homozygous UNC80 variant in a child with infantile hypotonia with psychomotor retardation and characteristic facies-2 (IHPRF2). *Metab. Brain Dis.* **33**, 869–873 (2018).
- He, Y. et al. Biallelic UNC80 mutations caused infantile hypotonia with psychomotor retardation and characteristic facies 2 in two Chinese patients with variable phenotypes. *Gene* **660**, 13–17 (2018).
- Zerangue, N., Schwappach, B., Jan, Y. N. & Jan, L. Y. A new ER trafficking signal regulates the subunit stoichiometry of plasma membrane K(ATP) channels. *Neuron* **22**, 537–548 (1999).
- Kschonsak, M. et al. Structural architecture of the human NALCN channelosome. *Nature* <https://doi.org/10.1038/s41586-021-04313-5> (2021).
- Li, N. et al. Structure of a pancreatic ATP-sensitive potassium channel. *Cell* **168**, 101–110 e110 (2017).
- Zheng, S. Q. et al. MotionCor2: anisotropic correction of beam-induced motion for improved cryo-electron microscopy. *Nat. Methods* **14**, 331–332 (2017).
- Zhang, K. Gctf: real-time CTF determination and correction. *J. Struct. Biol.* **193**, 1–12 (2016).
- Zivanov, J. et al. New tools for automated high-resolution cryo-EM structure determination in RELION-3. *Elife* <https://doi.org/10.7554/eLife.42166> (2018).
- Punjani, A., Rubinstein, J. L., Fleet, D. J. & Brubaker, M. A. cryoSPARC: algorithms for rapid unsupervised cryo-EM structure determination. *Nat. Methods* **14**, 290–296 (2017).
- Punjani, A., Zhang, H. & Fleet, D. J. Non-uniform refinement: adaptive regularization improves single-particle cryo-EM reconstruction. *Nat. Methods* **17**, 1214–1221 (2020).
- Wang, N. et al. Structural basis of human monocarboxylate transporter 1 inhibition by anti-cancer drug candidates. *Cell* **184**, 370–383 e313 (2021).
- Petersen, E. F. et al. UCSF Chimera—a visualization system for exploratory research and analysis. *J. Comput. Chem.* **25**, 1605–1612 (2004).
- Emsley, P., Lohkamp, B., Scott, W. G. & Cowtan, K. Features and development of Coot. *Acta Crystallogr. D. Biol. Crystallogr.* **66**, 486–501 (2010).
- Pfaff, J., Phan, N. M. & Si, D. DeepTracer for fast de novo cryo-EM protein structure modeling and special studies on CoV-related complexes. *Proc. Natl Acad. Sci. USA* <https://doi.org/10.1073/pnas.2017525118> (2021).
- Afonine, P. V. et al. Real-space refinement in PHENIX for cryo-EM and crystallography. *Acta Crystallogr. D. Struct. Biol.* **74**, 531–544 (2018).
- Petersen, E. F. et al. UCSF ChimeraX: structure visualization for researchers, educators, and developers. *Protein Sci.* <https://doi.org/10.1002/pro.3943> (2020).

41. Larkin, M. A. et al. Clustal W and Clustal X version 2.0. *Bioinformatics* **23**, 2947–2948 (2007).
42. Robert, X. & Gouet, P. Deciphering key features in protein structures with the new ENDscript server. *Nucleic Acids Res.* **42**, W320–W324 (2014).
43. Chen, S. et al. High-resolution noise substitution to measure overfitting and validate resolution in 3D structure determination by single particle electron cryomicroscopy. *Ultramicroscopy* **135**, 24–35 (2013).

Acknowledgements

We thank Prof. Dejian Ren for providing the cDNA of hNALCN, rNALCN, mUNC80, and mUNC79. We thank all of Chen Lab members for kindly help. Cryo-EM data collection was supported by the Electron microscopy laboratory and the Cryo-EM platform of Peking University with the assistance of Xuemei Li, Zhenxi Guo, Changdong Qin, Xia Pei, and Guopeng Wang. Part of the structural computation was also performed on the Computing Platform of the Center for Life Science (Life Science No. 1) and the High-performance Computing Platform of Peking University (Wei-Ming No.1). We thank the National Center for Protein Sciences at Peking University in Beijing, China for assistance with negative stain EM. The work is supported by grants from the National Natural Science Foundation of China (91957201, 31870833, and 31821091 to L.C.) and Center For Life Sciences (CLS). Y.K. is supported by the Boya Postdoctoral Fellowship of Peking University.

Author contributions

L.C. initiated the project and wrote the manuscript draft. Y.K. carried out experiments with the help of L.C. Both authors contributed to the manuscript preparation.

Competing interests

The authors declare no competing interests.

Additional information

Supplementary information The online version contains supplementary material available at <https://doi.org/10.1038/s41467-022-30403-7>.

Correspondence and requests for materials should be addressed to Lei Chen.

Peer review information *Nature Communications* thanks Xiaochen Bai and the other, anonymous, reviewer(s) for their contribution to the peer review of this work.

Reprints and permission information is available at <http://www.nature.com/reprints>

Publisher's note Springer Nature remains neutral with regard to jurisdictional claims in published maps and institutional affiliations.



Open Access This article is licensed under a Creative Commons Attribution 4.0 International License, which permits use, sharing, adaptation, distribution and reproduction in any medium or format, as long as you give appropriate credit to the original author(s) and the source, provide a link to the Creative Commons license, and indicate if changes were made. The images or other third party material in this article are included in the article's Creative Commons license, unless indicated otherwise in a credit line to the material. If material is not included in the article's Creative Commons license and your intended use is not permitted by statutory regulation or exceeds the permitted use, you will need to obtain permission directly from the copyright holder. To view a copy of this license, visit <http://creativecommons.org/licenses/by/4.0/>.

© The Author(s) 2022